DOE/PC/91008--23-Pt.4

Mechanical Failure of Cavities in Poroelastic Media

G. Ozkan and P. Ortoleva

Laboratory for Computational Geodynamics
Department of Chemistry
Indiana University
Bloomington, Indiana 47405

Table of Contents

Abstract

The stress-induced failure of cavities in poroelastic media is investigated using an analytical solution of the elastic matrix inclusion problem of Eshelby and a rock failure criterion. The elastic properties of the porous matrix surrounding the cavity are modeled using a self-consistent version of the theory of Berryman while the cavity collapse criterion is based on a failure condition calibrated as a function of matrix mineralogy, grain size and porosity. The influence of the latter textural variables as well as pore fluid pressure and cavity shape and orientation relative to the far-field stress are evaluated. The region of failure on the cavity surface is identified. These results are applied to the prediction of vug stability in a sedimentary basin in the context of vuggy reservoir exploration and production.

INTRODUCTION

Cavities in porous media form as a result of natural and engineering processes. The issue of their mechanical stability is central to applications in petroleum exploration and production, materials engineering, civil engineering, and basic geoscience. Examples include cavitation created due to excessive matrix acidizing treatments, the prediction of vuggy reservoir location and characteristics, and the analysis of karsts and magma chambers. Failure or survival of a cavity is determined by far-field stress, cavity geometry and orientation relative to the far-field stress, fluid pressures inside the cavity and in the surrounding matrix, and the textural properties of the surrounding matrix. The latter include porosity and grain sizes and associated mechanical properties. For multi-phase systems, capillarity and wetting also could affect the cavity stability.

The purpose of the present study is to assess the stresses at the surface of a cavity inside a porous matrix and use it to set forth a criterion for failure/collapse of the cavity. The dimensions of the cavities of interest are much larger than the matrix grain sizes. The fluid pressure inside the cavity is assumed to be equal to the matrix fluid pressure. Only the single-phase aspects of the problem are addressed in this study.

Eshelby (1957) determined the stress inside and just outside of an ellipsoidal, pore-free elastic inclusion in an infinite elastic, pore-free medium subjected to a far-field stress. In this study, these results were generalized and the stress at the surface of the ellipsoidal cavity inside a poroelastic media were obtained.

Poroelasticity coefficients of the surrounding porous matrix, which is composed of several minerals, were calculated using the self-consistent effective medium approximation of Berryman (1986). For the stability analysis, Drucker-Prager failure criterion was used (Drucker and Prager, 1952) with calibrated parameters. In Sakrani (1996), these parameters were calibrated with rock mechanics data and empirical relations for the dependence on rock texture were setforth. Parametric studies of the stability of ellipsoidal cavities was performed to understand the nature of failure phenomena. The vug stability analysis was done for a homogeneous and a layered basin under overburden stresses and vug survival-depth curves were obtained.

CAVITY IN A POROELASTIC MEDIUM

Consider the computation of the stress around a cavity in a poroelastic medium. Let Λ be the tensor of poroelastic coefficients. Then the strain tensor ε and stress tensor σ are related by

$$\sigma_{ij} + \alpha p \delta_{ij} = \Lambda_{ijmn} \varepsilon_{mn} \tag{1}$$

for effective stress coefficient α, and pore fluid pressure p. In Eq.(1), standard indicial notation is used with the summation convention on repeated indices, all indices are within the range 1-3 and δ_{ij} is the Kronecker delta. The boundary conditions adopted are that the

normal stress at the cavity surface is $-p$, tangential shear is zero and that $\sigma \to \sigma^{\infty}$ stress far from the cavity.

Let $\Sigma^E(\sigma^{\infty})$ be a solution of the aforementioned problem for $p=0$. Then the solution of the problem of interest here has been shown in Sakrani (1996) and Sakrani and Ortoleva (1997) :

$$\sigma_{ij} = \Sigma^E_{ijmn}(\sigma^{\infty}_{mn} + p\delta_{mn}) - p\delta_{ij} \ . \tag{2}$$

This result holds for voids of arbitrary shape as long as the tensor Σ^E is known for that shape.

In this study, the cavity is assumed to be an ellipsoid as seen in Fig.1. The x_i - coordinate system lies along the principal axes of the ellipsoid (dashed lines in Fig.1). According to this coordinate system, the surface of the ellipsoid can be written as

$$\frac{{x_1}^2}{a^2} + \frac{{x_2}^2}{b^2} + \frac{{x_3}^2}{c^2} = 1 \tag{3}$$

where a, b and c are the principal dimensions. The poroelastic medium is assumed to be isotropic. With this

$$\sigma_{ij} + \alpha p\delta_{ij} = \lambda\varepsilon_{kk}\delta_{ij} + 2\mu\varepsilon_{ij} \tag{4}$$

where λ and μ are the Lame's constants. The Poisson's ratio ν is given by

$$\nu = \frac{\lambda}{2(\lambda+\mu)} \ . \tag{5}$$

Eshelby (1957) determined the stress inside and just outside of an ellipsoidal, pore-free inclusion in an infinite elastic, pore-free medium when the system was subjected to far-field stresses. Following this study, one can obtain the elastic fields at the surface of an ellipsoidal cavity under the influence of a far-field disturbance. The derivation is given in the Appendix. The strain tensor at the boundary of the cavity is found to be related to the far-field strain tensor by

$$\varepsilon_{ij} = \left(\delta_{ik}\delta_{jl} + \frac{1}{1-\nu}n_i n_j n_k n_l - \frac{\nu}{1-\nu}n_i n_j \delta_{kl} - n_k n_i \delta_{jl} - n_k n_j \delta_{il}\right) C_{klmn}\varepsilon^{\infty}_{mn} \ . \tag{6}$$

In Eq.(6), the n_i's are the components of the unit normal vector n at the boundary of the cavity as seen in Fig.1. The tensor C can be calculated from surface integrals of Kelvin solutions on the cavity surface; details are given in the Appendix.

By putting the strain tensor in vector form and using constitutive relations for p=0, the relation between the surface stresses and far-field stresses is obtained from Eq.(6) as

$$\sigma = \Lambda(I+N)C\Lambda^{-1}\sigma^{\infty} \tag{7}$$

where σ and σ^{∞} are the stress vectors at the boundary of and far from the cavity, respectively. The stress vector is a 6×1 column vector having the form

$$\sigma = \begin{bmatrix}\sigma_{11} & \sigma_{22} & \sigma_{33} & \sigma_{12} & \sigma_{13} & \sigma_{23}\end{bmatrix}^T$$

where superscript T denotes the transpose. In Eq.(7), I is the 6×6 identity matrix, Λ is the elasticity matrix for isotropic materials which can be written in terms of shear modulus μ and Poisson's ratio ν as

$$\Lambda = \frac{2\mu}{(1-2\nu)} \begin{bmatrix} 1-\nu & \nu & \nu & 0 & 0 & 0 \\ \nu & 1-\nu & \nu & 0 & 0 & 0 \\ \nu & \nu & 1-\nu & 0 & 0 & 0 \\ 0 & 0 & 0 & 1-2\nu & 0 & 0 \\ 0 & 0 & 0 & 0 & 1-2\nu & 0 \\ 0 & 0 & 0 & 0 & 0 & 1-2\nu \end{bmatrix} . \tag{8}$$

The matrix C in Eq.(6) is the inverse of a 6×6 matrix which depends on the elements S_{ijkl} via Eq.(9) (see the Appendix for S_{ijkl}).

$$C = \begin{bmatrix} 1-S_{1111} & S_{1122} & S_{1133} & 0 & 0 & 0 \\ S_{2211} & 1-S_{2222} & S_{2233} & 0 & 0 & 0 \\ S_{3311} & S_{3322} & 1-S_{3333} & 0 & 0 & 0 \\ 0 & 0 & 0 & 1-2S_{1212} & 0 & 0 \\ 0 & 0 & 0 & 0 & 1-S_{1313} & 0 \\ 0 & 0 & 0 & 0 & 0 & 1-S_{2323} \end{bmatrix}^{-1} . \tag{9}$$

Finally, in Eq.(6), N is the 6×6 matrix which specifies the position on the cavity surface at which the stresses are to be calculated. It has the form given in Eq.(10).

$$N = \frac{1}{1-\nu} \begin{bmatrix} n_1^4 & n_1^2 n_2^2 & n_1^2 n_3^2 & 2n_1^3 n_2 & 2n_1^3 n_3 & 2n_1^2 n_2 n_3 \\ n_1^2 n_2^2 & n_2^4 & n_2^2 n_3^2 & 2n_1 n_2^3 & 2n_1 n_2^2 n_3 & 2n_2^3 n_3 \\ n_1^2 n_3^2 & n_2^2 n_3^2 & n_3^4 & 2n_1 n_2 n_3^2 & 2n_1 n_3^3 & 2n_2 n_3^3 \\ n_1^3 n_2 & n_1 n_2^3 & n_1 n_2 n_3^2 & 2n_1^2 n_2^2 & 2n_1^2 n_2 n_3 & 2n_1 n_2^2 n_3 \\ n_1^3 n_3 & n_1 n_2^2 n_3 & n_1 n_3^3 & 2n_1^2 n_2 n_3 & 2n_1^2 n_3^2 & 2n_1 n_2 n_3^2 \\ n_1^2 n_2 n_3 & n_2^3 n_3 & n_2 n_3^3 & 2n_1 n_2^2 n_3 & 2n_1 n_2 n_3^2 & 2n_2^2 n_3^2 \end{bmatrix}$$

$$-\frac{\nu}{1-\nu} \begin{bmatrix} n_1^2 & n_1^2 & n_1^2 & 0 & 0 & 0 \\ n_2^2 & n_2^2 & n_2^2 & 0 & 0 & 0 \\ n_3^2 & n_3^2 & n_3^2 & 0 & 0 & 0 \\ n_1 n_2 & n_1 n_2 & n_1 n_2 & 0 & 0 & 0 \\ n_1 n_3 & n_1 n_3 & n_1 n_3 & 0 & 0 & 0 \\ n_2 n_3 & n_2 n_3 & n_2 n_3 & 0 & 0 & 0 \end{bmatrix} - \begin{bmatrix} 2n_1^2 & 0 & 0 & 2n_1 n_2 & 2n_1 n_3 & 0 \\ 0 & 2n_2^2 & 0 & 2n_1 n_2 & 0 & 2n_2 n_3 \\ 0 & 0 & 2n_3^2 & 0 & 2n_1 n_3 & 2n_2 n_3 \\ n_1 n_2 & n_1 n_2 & 0 & n_1^2 + n_2^2 & n_2 n_3 & n_1 n_3 \\ n_1 n_3 & 0 & n_1 n_3 & n_2 n_3 & n_1^2 + n_3^2 & n_1 n_2 \\ 0 & n_2 n_3 & n_2 n_3 & n_1 n_3 & n_1 n_2 & n_2^2 + n_3^2 \end{bmatrix} \tag{10}$$

We can now define the Eshelby matrix, σ^E, which transforms the far-field stresses to the stresses at the boundary of the ellipsoidal cavity. From Eq.(6), the Eshelby matrix is found to be

$$\sigma^E = \Lambda(I+N)C\Lambda^{-1} . \tag{11}$$

The stress vector σ at the boundary is obtained bu applying the Eshelby matrix to the far-field stress vector.

In this study, a computer code was developed to calculate the analytical expressions in the matrix C and to evaluate the Eshelby matrix. The surface integrals for S_{ijkl} were calculated numerically by subdividing the domain and using a 10 point Gaussian integration in each subdomain. The numerical scheme was checked with the analytical closed form solutions for spherical cavities given in Eshelby (1957). The results of our numerical scheme and the analytical ones agree within the machine accuracy.

After the Eshelby matrix is calculated via Eq.(11), for cavities in porous media, the stress vector at the surface of ellipsoidal cavity can be evaluated according to Eq.(2). This equation can be written in the vector form

$$\begin{bmatrix} \sigma_{11} \\ \sigma_{22} \\ \sigma_{33} \\ \sigma_{12} \\ \sigma_{13} \\ \sigma_{23} \end{bmatrix} = \sigma^E \cdot \begin{bmatrix} \sigma_{11}^{\infty} + p \\ \sigma_{22}^{\infty} + p \\ \sigma_{33}^{\infty} + p \\ \sigma_{12}^{\infty} \\ \sigma_{13}^{\infty} \\ \sigma_{23}^{\infty} \end{bmatrix} - \begin{bmatrix} p \\ p \\ p \\ 0 \\ 0 \\ 0 \end{bmatrix}. \tag{12}$$

The elastic coefficients λ, μ and ν depend the texture of the porous matrix. When the matrix is composed of grains of several minerals, these coefficients are approximated here by the effective medium approximations (Berryman, 1986).

Effective Medium Approximation for Porous Matrices

The effective medium approximation for porous matrices has been studied in Berryman (1986). Using his formulae and the self consistent approximation, the averaged (effective) bulk and shear moduli of the matrix and the effective stress parameter can be evaluated. Let the porous matrix be composed of N_c solid constituents of volume fractions ϕ_i and porosity ϕ (the void phase is the $(N_c+1)^{\text{th}}$ constituent, i.e., $\phi = \phi_{N_c+1}$). The self consistent approximation formulae are

$$\frac{1}{\kappa^* + \frac{4}{3}\mu^*} = \sum_{i=1}^{N_c+1} \frac{\phi_i}{\kappa_i + \frac{4}{3}\mu^*} \tag{13}$$

$$\frac{1}{F^* + \mu^*} = \sum_{i=1}^{N_c+1} \frac{\phi_i}{F^* + \mu_i} \tag{14}$$

where κ_i and μ_i are bulk and shear moduli of constituent i, while the variables with superscript * are the effective medium parameters of interest. In isotropic materials, the bulk modulus can be expressed in terms of Lame's constants as

$$\kappa = \lambda + \frac{2}{3}\mu. \tag{15}$$

F^* in Eq.(14) is given in Berryman (1986) in the form

$$F^* = \frac{\mu^*}{6}\frac{9\kappa^* + 8\mu^*}{\kappa^* + 2\mu^*}. \tag{16}$$

The nonlinear system of equations for two unknowns (effective bulk and shear moduli of the matrix) formed by Eqs.(13) and (14) can be solved numerically. Since the shear and bulk moduli of the void phase are zero, numerical singularity may arise in this

system for some porosity values. Berryman (1980) studied the singularity of this system for two phase matrices, when one phase has very small (or zero) shear modulus. Following his method, we define a new variable χ as

$$\chi = \frac{1}{6}\frac{9\kappa^* + 8\mu^*}{\kappa^* + 2\mu^*} \qquad \frac{2}{3} \le \chi \le \frac{3}{2} \tag{17}$$

and after some mathematical manipulations, reformulate the system of equations as

$$\frac{1}{1+\chi} = \sum_{i=1}^{N_c} \frac{\phi_i \mu_i}{\mu_i + \chi\mu^*}$$

$$\frac{3\chi - 2}{1+\chi} = \sum_{i=1}^{N_c} \frac{\phi_i \kappa_i}{\kappa_i + \frac{4}{3}\mu^*} \tag{18}$$

χ and μ^* can be evaluated from Eqs.(18) without any numerical difficulty. The effective bulk modulus is then obtained from

$$\kappa^* = \frac{4}{3}\mu^* \frac{3\chi - 2}{3 - 2\chi} . \tag{19}$$

According to Berryman (1986), the effective stress parameter of the matrix can be approximated by

$$\frac{\alpha^*}{\kappa^* + \frac{4}{3}\mu^*} = \sum_{i=1}^{N_c+1} \frac{\phi_i \alpha_i}{\kappa_i + \frac{4}{3}\mu^*} \tag{20}$$

where α_i is the effective stress parameter of the i^{th} constituent and can be calculated from

$$\alpha_i = 1 - \frac{\kappa_i}{(\kappa_s)_i} \tag{21}$$

where $(\kappa_s)_i$ is the bulk modulus of the grain when the grain has no pores in it. The values of α_i vary between 0 and 1 corresponding to the pure solid grains and void cases, respectively. In this study, we consider pure solid grains only and the effective stress coefficient for solid grains in a porous matrix can be calculated as

$$\frac{\alpha^*}{\kappa^* + \frac{4}{3}\mu^*} = \frac{\phi}{\frac{4}{3}\mu^*} . \tag{22}$$

To simplify the notation, we omit * from the bulk modulus, shear modulus and effective stress parameter, henceforth.

Failure/Collapse Criterion

The computations of stress at the surface of the cavity, in conjunction with a rock failure criterion, allow us to estimate conditions under which the material around the cavity will fail. This calculation thereby is an estimate of the critical conditions for cavity collapse. Let σ be the stress tensor at the point P on the cavity surface. Then failure will occur when a function F just exceeds zero:

$$F(\sigma, p, \Theta) > 0 \quad , \quad \text{collapse.} \tag{23}$$

Here Θ is the texture (porosity, mineral volume fractions and grain sizes) of the porous matrix. From the poroelastic modified Eshelby solution, we see that σ depends on σ^{∞}, p, Θ, and the position of the boundary point P. Note that failure will occur under different conditions for different points on the cavity surface. Hence Eq.(23), the failure criterion, can be rewritten

$$F(\sigma^{\infty}, p, \Theta, \mathrm{P}, \omega) = \mathrm{F}(\sigma, p, \Theta). \tag{24}$$

Finally, ω represents a set of angles orienting the cavity relative to the principle axes of far-field stress σ^{∞} (see Fig.1).

To calculate F, we use the Drucker-Prager failure criterion in the form

$$F = \sqrt{J_2} + \mathrm{a}(\Theta) J_1 - \mathrm{b}(\Theta) \tag{25}$$

where J_1 and J_2 are the first and second invariants of the effective stress tensor σ^{eff} ($\sigma^{eff} = \sigma + \alpha p I$) at the cavity surface and can be calculated from

$$J_1 = tr(\sigma^{eff})$$

$$J_2 = \frac{1}{2} tr\left((\sigma^{eff} - \frac{J_1}{3} I)^2 \right) \tag{26}$$

The coefficients a and b in Eq.(25) depend on texture Θ. In Sakrani (1996), these parameters are calibrated with rock mechanics data and their relation to matrix porosity, constituent grain sizes and volumetric ratios is given.

Failure commences when F is just equal to zero at a point, curve or simultaneously over all the cavity surface as some parameter passes through a critical value. The spatial dimension of the failure zone depends on a number of factors, such as, the anisotropy of σ^{∞}, the cavity geometry and orientation with respect to the principal axes of far-field stress. Qualitatively speaking, the dimension increases with the symmetry of the problem. Nonetheless, the failure threshold for the cavity depends on the first indicated failure somewhere on the cavity surface.

CAVITY STABILITY IN CARBONATE MATRICES

The developments of the previous section can be integrated to study cavity stability in carbonate matrices. The porous carbonate matrix is composed of solid calcite and dolomite grains. In the matrix, there is an ellipsoidal cavity which is subjected to the far-field stress tensor σ^{∞} as seen in Fig.1. A constant fluid pressure is assumed within the porous matrix and inside the cavity.

For calcite-dolomite matrices, the Drucker-Prager failure criterion coefficients a(Θ) and b(Θ) are given in Sakrani (1996) as

$$a(\Theta) = \sum_i f_i a_i$$

$$b(\Theta) = \sum_i f_i b_i \tag{27}$$

where f_i is the matrix volume fraction of mineral i(i=calcite, dolomite), i.e., $f_i=\phi_i/1-\phi$ and the coefficients a_i and b_i are

$$a_{calcite} = 0.2782 R_{calcite}^{-0.0068} e^{-6.874\phi}$$

$$a_{dolomite} = 0.5673 R_{dolomite}^{0.0669} e^{-22.727\phi}$$

$$b_{calcite} = 44.7655 R_{calcite}^{-0.1956} e^{-4.0615\phi} \tag{28}$$

$$b_{dolomite} = 49.1584 R_{dolomite}^{-0.2225} e^{-8.9871\phi}$$

In Eqs.(28) R_i is the grain size (mm) of mineral i, and b_i is in MPa. The values used in this study are

$$f_{calcite} = f_{dolomite} \quad , \quad R_{calcite} = R_{dolomite} = 0.1mm. \tag{29}$$

To calculate effective medium parameters of porous calcite-dolomite composites, we use the material bulk and shear moduli of pure calcite and dolomite grains. Values for physical properties of minerals and rocks can be found in Clark (1966). The isotropic elastic constants for calcite and dolomite are evaluated from this reference as

$$\kappa_{calcite} = 70 \text{ GPa} \qquad \mu_{calcite} = 28 \text{ GPa}$$

$$\kappa_{dolomite} = 85 \text{ GPa} \qquad \mu_{dolomite} = 37 \text{ GPa} \tag{30}$$

The material and failure coefficients of the matrix with these parameters are summarized in Table 1.

Table 1. Matrix elasticity and calibrated Drucker-Prager coefficients of the porous matrix defined in Eqs.(29) and (30) for different porosity values.

ϕ	ν	α	a(Θ)	b(Θ) (MPa)
0.05	*0.309*	*0.136*	*0.178*	*54.84*
0.10	*0.301*	*0.263*	*0.096*	*40.10*
0.15	*0.292*	*0.383*	*0.058*	*29.75*
0.20	*0.283*	*0.495*	*0.038*	*22.39*

As seen from the table, the effective stress parameter α increases significantly, whereas Poisson's ratio is not strongly affected by porosity. The limits for the effective stress parameters are *0* and *1*, corresponding to ϕ=*0* (no porosity) and ϕ=*1* (hypothetical no matrix case). As the porosity of the medium increases, the failure parameters a and b

will decrease. Because b(Θ) decreases with increasing porosities, the failure will occur at lower stress states for higher porosity. The failure parameter a(Θ) introduces the favorable effects of normal stresses to the cavity stability (when the normal stresses are compressive). Therefore, as the porosity of the medium decreases, the contribution of normal stresses to stability increases.

The principal dimensions of the ellipsoid are denoted *a, b* and *c* respectively. In this study, to reduce one of the parameters, two minor dimensions are set equal via

$$a \geq b = c \tag{31}$$

and the aspect ratio of the ellipsoid, ε, is defined as (b/a) ratio.

The cavity deforms under the effect of the fluid pressure p and far-field stress. The principal axes of the far-field stress tensor σ^{∞} will define the *XYZ* system as shown in Fig.1. Thus, the far-field stress vector has the form

$$\sigma^{\infty} = \left[-\sigma_X^{\infty} \quad -\sigma_Y^{\infty} \quad -\sigma_Z^{\infty} \quad 0 \quad 0 \quad 0\right]^T \tag{32}$$

where σ_X^{∞}, σ_Y^{∞} and σ_Z^{∞} are the principal compressive stresses in the *X*, *Y* and *Z* directions, respectively. In this study, we set the stresses in the *X* and *Y* directions equal:

$$\sigma_Z^{\infty} \geq \sigma_X^{\infty} = \sigma_Y^{\infty} \tag{33}$$

and define the far-field stress anisotropy ratio $\sigma_X^{\infty}/\sigma_Z^{\infty}$.

The cavity orientation is defined by the principal axes of the ellipsoid ($x_1x_2x_3$ frame) with respect to the principal axes of σ^{∞} (*XYZ* frame). Since b=c and $\sigma_X^{\infty} = \sigma_Y^{\infty}$, the cavity orientation ω is the angle between *Z* and x_3 axes (Fig.1). ω=*0* represents the orientation in which the major principal axis of the cavity (x_1 axis) is perpendicular to the major principal stress axis (*Z* axis), whereas ω=π/2 represents the parallel case. Cavities having these orientations are called horizontal and vertical cavities, respectively.

In cavity stability calculations, the failure function *F* is determined from Eq.(25) at every point of the surface. Failure stress corresponds to the smallest σ_Z^{∞} value at which *F* is equal to zero for at least one point. For the most symmetric case (spherical cavity and hydrostatic far-field stress), failure happens everywhere on the surface of the sphere simultaneously.

In Fig.2, a series of *F* distributions on the cavity surface is presented for the ellipsoidal cavity with ε=*0.5*. The porous continuum has the matrix texture defined in Eqs.(29) and (30) with porosity ϕ=*0.2*. This texture yields the poroelastic and failure coefficients given in the last row of Table 1. The fluid pressure and far field stress anisotropy ratio are taken to be p=5MPa and $\sigma_X^{\infty}/\sigma_Z^{\infty}$=*0.5*.

In Fig.2a, the distribution of *F* is plotted for the horizontal cavity. The failure stress is max(σ_Z^{∞})=*27.40* MPa for this orientation and the failure function at this stress state is changing in the range (*-20.76, 0*) MPa on the surface. Failure occurs at two points with coordinates $(0, \pm 0.5a, 0)$ in the *XYZ* frame. Fig.2b and Fig.2c show the dependence of *F* on cavity orientation. In case b with ω=π/*6*, the failure stress is *29.66* MPa and failure occurs at points (±*0.898a, 0,* ±*0.410a*). In case c with ω=π/*3*, the failure stress level increases to *36.86* MPa and the coordinates of failure points are (±*0.647a, 0,* ±*0.638a*).

Fig.2d presents the vertical cavity for which the failure stress is $\max(\sigma_Z^\infty)$=*44.61* MPa and the failure function has the range (*-12.14*, *0*) MPa on the cavity surface. Due to the symmetry of cavity geometry in the *XY* plane, failure occurs along equatorial circle of radius *b*.

In Fig.3, the variations of failure stress of an ellipsoidal cavity (*b/a=0.5*) with porosity and fluid pressures are given. In the calculations, the matrix texture is taken as in Eqs.(29) and (30). The far-field stress anisotropy ratio is $\sigma_X^\infty/\sigma_Z^\infty$=*0.5*. As is seen from the graph, the cavities in the matrix with higher porosity fail at lower stresses than do those in a lower porosity matrix. For a fixed porosity, as the fluid pressure of the system increases, failure stress increases and the cavity becomes more stable. The increase in the cavity stability due to fluid pressure is independent of the porosity of the medium.

The changes in failure stress with cavity shape and orientation are presented graphically in Fig.4, for the fixed stress anisotropy level ($\sigma_X^\infty/\sigma_Z^\infty$=*0.5*) and fluid pressure (*p=5* MPa). The matrix texture is as in Eqs.(29) and (30) and porosity is taken to be *0.2*. With these parameters, spherical cavities fail at *32.57* MPa. Horizontal cavities fail at lower stresses than those for spheres and the failure stress values are ordered according to their aspect ratios, as seen in Fig.4. On the other hand, vertical cavities fail at higher stress levels than those for spheres and their failure stresses increase with decreasing aspect ratio of the ellipsoid. The vertical cavity with *b/a=0.2* withstands far-field stresses up to $\max(\sigma_Z^\infty)$=*51.17* MPa. Ellipsoidal cavities become more stable as they become more vertical.

In Fig.5a, b, and c, failure diagrams (in terms of the variation of failure stress $\max(\sigma_Z^\infty)$ with lateral stress σ_X^∞) are shown for spherical and ellipsoidal (*b/a=0.5)* cavities. In the calculations, matrix texture is taken as in Eqs.(29) and (30) with porosity ϕ=*0.2*. Fluid pressure is kept constant at *p=5* MPa. In these diagrams, there are finite survival zones bounded by two failure envelopes that can be identified with vertical stress and lateral stress-dominated failure mechanisms. The vertical stress-dominated failure curve determines the upper boundary of the survival zone, whereas the lateral stress-dominated boundary bounds the survival zone from below.

For spherical cavities (Fig.5a), the upper boundary starts at $\max(\sigma_Z^\infty)$= *22.8* MPa when there is no lateral stress. Failure occurs along the equatorial circle of the sphere; as the lateral stress increases, the sphere becomes more stable up to the hydrostatic stress state of *35.2* MPa. When the lateral stress is greater than this value, the sphere fails at its poles, as is indicated in Fig.5a. At the $\sigma_Z^\infty = 0$ termination of the lateral failure boundary curve, the lateral stress is *23.7* MPa and failure occurs along the equatorial circle. There appears to be a finite (but short) segment of this lateral failure curve that extends from the $\sigma_Z^\infty = 0$ termination of the lateral failure curve to the point where the slope of that curve changes discontinuously.

The survival zone for vertical ellipsoids is seen in Fig. 5b. The survival zone boundary is similar to that for the sphere. When vertical stress dominates, failure occurs on the equatorial circle whereas, for the lateral stress-dominated case, the poles are the sites of failure. The vertical stress-dominated failure boundary curve starts at $\max(\sigma_Z^\infty)$=

29.3 MPa for zero lateral stress and the failure lateral stress is *22.1* MPa when there is no vertical stress. When the lateral stress reaches *31.5* MPa, the failure mode changes from equatorial circle failure to polar, point failure by a small change in conditions ($\sigma_X^\infty, \sigma_Z^\infty$).

For the horizontal ellipsoid, both vertical and horizontal stress-dominated failures are by isolated point failure as indicated in Fig.5c. The position of failure points on the cavity surface changes at points of tangent discontinuity of the curve bounding the survival zone. The vertical stress-dominated failure boundary of the survival zone starts at max(σ_Z^∞)= *19.2* MPa when there is no lateral stress. In this case, failure occurs at the poles. As the lateral stress increases, the failure point switches from poles, to lateral equatorial points and back to the poles as suggested in Fig. 5c. The horizontal failure curve appears to consist of two linear segments. For smaller vertical stresses the points of failure are at the poles while for the upper linear segment, failure occurs at the top and bottom lateral equatorial points.

Breaks in slope of the survival zone boundary curve correspond to failure mode transition points (i.e., isolated stress states at which two modes of failure occur simultaneously). For the horizontal cavity, the vertical and horizontal failure envelopes meet at the *31.6* MPa lateral stress. At that point, the vertical stress of *24.6* MPa yields to failure at the poles, but when the vertical stress decreases to *24.4* MPa, the failure points switch to the lateral equatorial positions. In Fig.5d, the variation of failure function along the cavity surface at this critical stress state ($\sigma_X^\infty = 31.6$ MPa , where the $\sigma_Z^\infty = 24.6$ MPa) is given in three-dimensional perspective. As is seen in Fig.5d, the region where the failure function exceeds zero extends from the poles to the lateral equatorial points. On that vertical pole-to-pole ellipse, values of the failure function are greater than zero at the points near the poles and very close to zero elsewhere along this curve. This figure suggests that, the transition between the two modes of point failure is through line failure.

From the above numerical results a general picture seems to emerge. A cavity survival zone exists in the space of constraints (σ_X^∞, σ_Z^∞, p, texture, etc.). This zone is bounded by a set of hypersurfaces each of which corresponds to a failure mode. For symmetric cavities (such as spheroids) the hypersurfaces join at conditions of high symmetry (for example $\sigma_X^\infty = \sigma_Z^\infty$ for a sphere). The horizontal cavity illustrates the fact that while discontinuities in the slope of the boundary curve indicate a switch in the location of the failure points, such switching can occur in the absence of such a discontinuity. Finally, we conjecture that for low symmetry cavities, point failure (and not line or full surface failure) is the dominant mode.

VUG STABILITY WITHIN A BASIN

Vugs (natural cavities) are important for petroleum reservoir characteristics. Our analysis shows that the many system parameters interact in complex ways to produce

vug stability/instability to collapse/failure. The vug stability criteria is obtained in terms of basic parameters characterizing the internal state of a basin or reservoir system.

Our vug collapse criterion allows for the prediction of the range of stability of vuggy reservoirs. Our analysis predicts the range of vug stability in terms of vug shape, orientation, far-field stress, fluid pressure and matrix texture. If the distribution of these parameters are known, then zones of vug stability within a basin can be delineated.

To illustrate the nature of vug stability within a basin, consider the case of no net lateral basin compression/extension and assess basin stresses via a purely poroelastic model. This one-dimensional problem can be solved exactly. The ratio of lateral stress to vertical stress (stress anisotropy ratio) at the depth d can be expressed in terms of fluid pressure and vertical stress at that depth as

$$\frac{\sigma_X^\infty}{\sigma_Z^\infty} = \frac{\nu}{1-\nu} + \frac{1-2\nu}{1-\nu}\alpha\frac{p}{\sigma_Z^\infty}. \tag{34}$$

σ_X^∞ and σ_Z^∞ in the above equation are the principal compressive stresses as defined in Eq.(32). For the simple case wherein the fluid pressure is hydrostatic and the fluid mass density has a constant value ρ_f then $p = \rho_f g d + 0.1$MPa (for gravitational acceleration g and depth d). If the rock (matrix plus pore fluid) has constant mass density ρ_r then one can evaluate vertical far-field stress and stress anisotropy ratio as

$$\sigma_Z^\infty = \rho_r g d$$

$$\frac{\sigma_X^\infty}{\sigma_Z^\infty} = \frac{\nu}{1-\nu} + \frac{1-2\nu}{1-\nu}\alpha\frac{\rho_f}{\rho_r} \tag{35}$$

These formulae allow for the analysis of the depth-dependence of vug stability for a normally (i.e. hydrostatic) fluid pressured regime.

Vug stability/depth curves for a homogeneous basin under the effect of overburden stresses and hydrostatic fluid pressure are shown in Fig.6. In this graph, depth is plotted against vug orientation for several ellipsoid aspect ratios. All other parameters (rock texture and mineralogy) are kept constant as in Eqs.(29) and (30) with porosity ϕ=0.2. The results of Fig.6 show the discrimination in the range of vug stability with respect to orientation and shape. For a given aspect ratio, the depth below which vugs are unstable depends strongly on orientation.

To analyze a particular basin or reservoir system all the above-cited parameters must be accounted for. Thus, we developed a computational module which taken as input matrix poroelastic constants, far-field stress, fluid pressure and vug orientation and shape and then gives a judgment on vug stability as the output.

In an actual system there is a statistical distribution of vug shapes and orientations: let ω be the vug orientation angle $\left(0 < \omega < \pi/2\right)$ and ε be the vug aspect ratio $\left(0 < \varepsilon < \infty\right)$. Let the vug distribution $\psi(\omega,\varepsilon)$ be defined as

$$\psi d\omega d\varepsilon = \text{fraction of vugs in } d\omega d\varepsilon.$$

Then the fraction of surviving vugs, x^s, is

$$x^s = \int_0^{\pi/2} d\omega \int_0^{\infty} d\varepsilon \psi(\omega,\varepsilon)\left[1-\vartheta(F)\right]. \qquad (36)$$

for $\vartheta(F)=1, F>0; 0, F<0$ where F is the vug failure criteria ($F>0$ for failure). From Fig.6 one may deduce that x^s starts as one at $d=0$, remains one for a depth interval, and then monotonically decreases to zero for the simple case of Fig.6. However, if fluid pressure is locally nonhydrostatic and as rock texture and mineralogy are not d-independent, it is seen that x^s can be a complex function of d.

A preliminary vug stability analysis was performed with lithological data obtained from Phillips Petroleum Company on the Midland Basin at the well location: longitude=102.8 and lattitude=32.2. At this location, the variations of lithology and mineralogy with depth are as in Tables 2 and 3.

For simplicity, in each formation brittle minerals, such as quartz, feldspars and chert, are combined in the dolomite group, whereas softer minerals are combined in the calcite group. The grain sizes of the calcite and dolomite groups are assumed to be equal to the average grain size of the corresponding formation. The original and current fluid pressures are taken from the field reports (data of Phillips Petroleum Company) surveying the region of longitude 102.6-102.8 and lattitude 32.06-32.22 (that includes the well from which the lithological data was obtained). The lateral stress ratio is calculated throughout depth assuming there was no lateral displacement (i.e., using formula 34).

The sequence of formations with depth, simplified rock texture and original (pre petroleum production) and current state fluid pressures in each formation are given in Fig.7. With these data, the vug survival analysis was performed for the Yates, San Andres, Clearfork, Simpson (McKee) and Ellenburger formations. The results are as follows.

- In the Yates formation, the spherical vugs within the lower 110 meters of the formation (i.e., below 1270 meters from the surface) are predicted to collapse. The survival curves for ellipsoidal vugs are similar to those in Fig.6, i.e., the vertical vugs survive deeper than spherical vugs do, whereas the horizontal ones collapse at shallower depths.
- In the San Andreas formation, current fluid pressures are much lower than the original ones. At the original state, all vugs survive at all depths within the formation. With the current state of fluid pressures, although spherical vugs do not collapse within the formation, horizontal or nearly horizontally oriented ones with aspect ratio $\varepsilon \leq 0.5$ do. Additional decrease in the fluid pressure will result in large scale vug collapse in this formation.
- In the Clearfork formation, all vugs survive at all depths within the formation for both the original and current state of fluid pressures.

Table 2. Lithology and thickness of formations at the well location longitude=102.8 and lattitude=32.2.

Geologic Age	Formation	Lithology	Thickness (m)
Quaternary		SS-Sh	170
Tertiary	Ogallala	Sandstone	175
Cretaceous		SS-LS	175
Triassic	Dockum	Shale1	170
Permian-Ochoan	Dewey-Lake	SS-Anhyd.	170
Permian-U.Guand.	Yates	Dolomite1	520
Permian-L.Guand.	San Andres	Dolomite3	630
Permian-Leonardian	Clearfork	Limestone	405
Permian-Wolfcamp	Wolfcamp	Limestone	15
Pennsylvanian	Atoka	Conglomer.	10
Mississipian	Barnett	Sh-LS	10
Devonian	Woodford	Shale3	110
Silurian	Fusselman	Dolomite4	110
Ordovician-Mohawkian	Simpson (McKee)	LS-Sh	50
Ordovician-Canadian	Ellenburger	Dolomite5	990

Table 3. Mineralogy of formations at the well location longitude=102.8 and lattitude=32.2.

Formation	Av.gr size (mm)	Quart	Felds.	Clays	Calcit.	Dolo.	Anhy.	Halite	Chert	Pyrite
Quaternary	0.60	0.60	0.10	0.30	0	0	0	0	0	0
Ogallala	1.10	0.92	0.03	0.05	0	0	0	0	0	0
Cretaceous	0.90	0.48	0.05	0.05	0.40	0.02	0	0	0	0
Dockum	0.035	0.30	0.05	0.65	0	0	0	0	0	0
Dewey-Lake	0.03	0.25	0.05	0.70	0	0	0	0	0	0
Yates	0.25	0.30	0.04	0.03	0.05	0.50	0.06	0	0.01	0.01
San Andres	0.20	0	0	0.08	0	0.80	0.09	0.01	0.02	0
Clearfork	0.15	0	0	0.15	0.60	0.15	0.08	0	0.02	0
Wolfcamp	0.20	0	0	0.35	0.55	0.04	0.05	0	0	0.01
Atoka	5.00	0.55	0.10	0.35	0	0	0	0	0	0
Barnett	0.15	0.04	0.01	0.35	0.60	0	0	0	0	0
Woodford	0.03	0.25	0.05	0.40	0	0	0	0	0.30	0
Fusselman	0.25	0	0	0.01	0.18	0.78	0	0	0.02	0.01
Simpson	0.20	0.23	0.02	0.25	0.48	0.01	0	0	0	0.01
Ellenburger	0.25	0	0	0.02	0.10	0.85	0.03	0	0	0

- In the Simpson (McKee) formation, for the original state of fluid pressures, most of the vugs survive except the horizontal ones with aspect ratio $\varepsilon \leq 0.3$. For the current state of fluid pressures which are much lower than the original ones, the sphere critical line is within the formation and the spherical vugs collapse in the lower 10 of the total 50 meters.
- In the Ellenburger formation, all vugs survive at all depths within the formation for both the original and current state of fluid pressures. But the current fluid pressure is very near to the limit of vug collapse. For example, when the current pressure is lowered by *1* MPa (such that, it is decreased from *9.65* MPa to *8.65* MPa at the top of the formation), the horizontal vugs with aspect ratio $\varepsilon < 0.2$ located near the bottom of the formation will collapse. Furthermore, the horizontal vugs with $\varepsilon = 0.1$ will collapse in the lower *70* meters of the formation.

Acknowledgment

We acknowledge Drs. K. Sundberg and M. Shebl for providing the data from the West Texas Permian Basin and the U.S. Department of Energy / BDM (contract # DE-AC22-94PC91008) and the U.S. Department of Energy / BES (contract # DE-FG02-91ER14175) for financial support.

APPENDIX

ELASTIC FIELDS AROUND AN ELLIPSOIDAL CAVITY

Eshelby (1957) determined the elastic fields inside and outside of an ellipsoid inclusion in an infinite medium by superposition of several strain fields. When the medium is isotropic the stress-strain relation has the form

$$\sigma_{ij} = 2\mu\left(\frac{\nu}{1-2\nu}\delta_{ij}\varepsilon_{kk} + \varepsilon_{ij}\right) \tag{A1}$$

where δ_{ij} is the Kronecker delta, λ is Lame's constant and ν is the Poisson's ratio. Eq.(A1) is written in indicial notation (all indices having the range 1-3) with the summation convention on repeated indices implied.

Consider an ellipsoidal inclusion referred to a rectangular x_i-frame (i=1-3) with origin at the center of the ellipsoid (see Fig.1). Following the work of Eshelby (1957), the "constrained" and "transformed" strain fields are related by

$$\varepsilon^c_{ij}(out) = \varepsilon^c_{ij}(in) + \frac{1}{1-\nu}n_i n_j n_k n_l \varepsilon^t_{kk} - \frac{\nu}{1-\nu}n_i n_j \varepsilon^t_{kk} - n_k(n_i\varepsilon^t_{jk} + n_j\varepsilon^t_{ik}) \tag{A2}$$

where ε^c_{ij} and ε^t_{ij} are the elements of "constrained" and "transformed" strain tensors, and (in) and (out) describe the fields inside and just outside the inclusion boundary, respectively. n_i is the i^{th} component of the unit normal at the boundary pointing inside the inclusion. The transformed strain is an arbitrary uniform strain whereas the constrained strain is the strain due to the applied transformed stress at the boundary of the inclusion while the boundary is constrained and can not have any displacements. The relation between constrained and transformed strains is

$$\varepsilon^c_{ij}(in) = S_{ijmn}\varepsilon^t_{mn} \tag{A3}$$

where S is a forth order tensor containing the spatial derivatives of the integral of the Kelvin solution over the ellipsoidal boundary. The elements of this tensor are

$$S_{ijkl} = \frac{1}{16\pi(1-\nu)}\int_0^{\pi}\int_0^{2\pi}\frac{\lambda_i g_{jkl} + \lambda_j g_{ikl}}{g}\sin\phi\, d\theta\, d\phi \tag{A4}$$

where

$$g_{ikl} = (1-2\nu)(\delta_{ik}r_l + \delta_{il}r_k - \delta_{kl}r_i) + 3r_i r_k r_l$$

$$\lambda_1 = \frac{r_1}{a^2} \quad , \quad \lambda_2 = \frac{r_2}{b^2} \quad , \quad \lambda_3 = \frac{r_3}{c^2}$$

$$g = \lambda_i r_i = \frac{r_1^2}{a^2} + \frac{r_2^2}{b^2} + \frac{r_3^2}{c^2}$$

$$(r_i) = (\sin\phi\cos\theta, \sin\phi\sin\theta, \cos\phi)$$

S depends only on ellipsoid geometry (a, b, c) and Poisson's ratio ν. From symmetry $S_{ijkl} = S_{jikl} = S_{ijlk}$. The non zero elements of S are

$$S_{11\underline{kk}} = \frac{1}{8\pi(1-\nu)a^2}\left[(2\delta_{1k}-1)(1-2\nu)I_1 + 3I_{1k}\right]$$

$$S_{22\underline{kk}} = \frac{1}{8\pi(1-\nu)b^2}\left[(2\delta_{2k}-1)(1-2\nu)I_2 + 3I_{2k}\right]$$

$$S_{33\underline{kk}} = \frac{1}{8\pi(1-\nu)c^2}\left[(2\delta_{3k}-1)(1-2\nu)I_3 + 3I_{3k}\right] \tag{A5}$$

$$S_{1212} = \frac{1}{16\pi(1-\nu)}\left[(1-2\nu)(\frac{I_1}{a^2}+\frac{I_2}{b^2}) + 3(\frac{1}{a^2}+\frac{1}{b^2})I_{12}\right]$$

$$S_{1313} = \frac{1}{16\pi(1-\nu)}\left[(1-2\nu)(\frac{I_1}{a^2}+\frac{I_3}{c^2}) + 3(\frac{1}{a^2}+\frac{1}{c^2})I_{13}\right]$$

$$S_{2323} = \frac{1}{16\pi(1-\nu)}\left[(1-2\nu)(\frac{I_2}{b^2}+\frac{I_3}{c^2}) + 3(\frac{1}{b^2}+\frac{1}{c^2})I_{23}\right]$$

where

$$I_i = \int_0^{\pi}\int_0^{2\pi}\frac{(r_i)^2}{g}\sin\phi d\theta d\phi$$

$$I_{\underline{ij}} = \int_0^{\pi}\int_0^{2\pi}\frac{(r_i r_j)^2}{g}\sin\phi d\theta d\phi \tag{A6}$$

and the underlined indices do not obey summation convention.

When a far-field strain (or stress) field ε^{∞} (or σ^{∞}) exists, the total strain just outside the inclusion is obtained by superposition

$$\varepsilon_{ij} = \varepsilon_{ij}^{c}(out) + \varepsilon_{ij}^{\infty} \tag{A7}$$

If there is a cavity instead of the inclusion, the stress continuity condition will yield a relation between far-field strain and transformed strains as

$$\varepsilon_{ij}^{c}(in) + \varepsilon_{ij}^{\infty} - \varepsilon_{ij}^{t} = 0 \tag{A8}$$

Using Eqs.(A2), (A7) and (A8), the elements of total strain tensor can then be expressed in terms of the transformed strain

$$\varepsilon_{ij} = \varepsilon_{ij}^{t} + \frac{1}{1-\nu}n_i n_j n_k n_l \varepsilon_{kk}^{t} - \frac{\nu}{1-\nu}n_i n_j \varepsilon_{kk}^{t} - n_k(n_i\varepsilon_{jk}^{t} + n_j\varepsilon_{ik}^{t}) \tag{A9}$$

and the relation between the transformed and far-field strains are obtained as

$$\varepsilon_{ij}^{\infty} = (\delta_{ik}\delta_{jl} - S_{ijkl})\varepsilon_{kl}^{t} \tag{A10}$$

(A10) leads to an inverse expression between transformed and far-field strain fields through a forth order tensor C in the form

$$\varepsilon_{ij}^{t} = C_{ijmn}\varepsilon_{mn}^{\infty} \tag{A11}$$

We can now express the strain field at the boundary of the cavity in terms of far-field strains

$$\varepsilon_{ij} = \left(\delta_{ik}\delta_{jl} + \frac{1}{1-\nu} n_i n_j n_k n_l - \frac{\nu}{1-\nu} n_i n_j \delta_{kl} - n_k n_i \delta_{jl} - n_k n_j \delta_{il} \right) C_{klrs} \varepsilon^{\infty}_{rs} \qquad \text{(A12)}$$

References

Berryman, J.G. (1980) Long-wavelength propagation in composite elastic media I. Spherical inclusions & II. Ellipsoidal inclusions, *J. Acoust. Soc. Am.* **68**, 1809-1831.

Berryman, J.G. (1986) Effective medium approximation for elastic constants of porous solids with microscopic heterogeneity, *J. Appl. Phys.* **59**, 1136-1140.

Clark, S.P.Jr. (ed.) (1966) *Handbook of Physical Constants, Revised Edition*, published by the Geological Society of America, #97.

Drucker, D.C. and Prager W. (1952) Soil mechanics and plastic analysis or limit design, *Quart. Appl. Math.* **10** , No: 2, 157-165.

Eshelby, J.D. (1957) The determination of the elastic field of an ellipsoid inclusion, and related problems, *Proceedings of the Royal Society of London A* **241**, 376-396.

Ozkan, G. and P. Ortoleva (1997) Multi-phase effects in material strength and cavity collapse criteria, in preparation.

Sakrani, K. (1996) A unified texture and mineralogy-dependent model for rock deformation, doctoral thesis, Indiana University.

Sakrani, K. and P. Ortoleva (1997) Vug collapse: An Eshelby, Drucker-Prager criterion, Quarterly report of *Naturally Fractured Reservoirs: Optimized E&P Strategies Using a Reaction-Transport-Mechanical Simulator in an Integrated Approach*, U.S. Department od Energy/BDM (Contract #: DE-AC22-94PC91008).

CAPTIONS OF FIGURES

Fig.1 Schematic ellipsoidal cavity in a poroelastic continuum with properties ν, α subjected to stress σ^{∞} applied far from the cavity.

Fig.2 Failure function values on the surface of the ellipsoidal cavity ($b/a=0.5$) at the failure state of stress. (a) horizontal cavity ($\omega=0$). (b) $\omega=\pi/6$. (c) $\omega=\pi/3$. (d) vertical cavity ($\omega=\pi/2$).

Fig.3 Variation of failure stress of an ellipsoidal cavity ($b/a=0.5$) with porosity and fluid pressure, at the stress anisotropy $\sigma_x^{\infty}/\sigma_z^{\infty}=0.5$.

Fig.4 Effect of cavity shape and orientation to the failure stress, at constant porosity $\phi=0.2$, fluid pressure $p=5$ MPa and stress anisotropy $\sigma_x^{\infty}/\sigma_z^{\infty}=0.5$.

Fig.5 Lateral versus vertical far-field stress failure envelopes for cavities in constant porosity $\phi=0.2$ and fluid pressure $p=5$ MPa. (a) spherical cavity, (b) vertical ellipsoidal cavity ($b/a=0.5$), (c) horizontal ellipsoidal cavity ($b/a=0.5$), (d) failure function on the surface of the horizontal ellipsoid at the failure mode transition zone.

Fig.6 Depth of survival curve for ellipsoidal vugs with different shape and orientations in a calcite-dolomite basin (ϕ=0.2) under overburden stresses and hydrostatic fluid pressure.

Fig.7 Sequence of formations, simplified rock texture and fluid pressures at each formation of the Midland basin at the well location: longitude=102.8, lattitude=32.2.

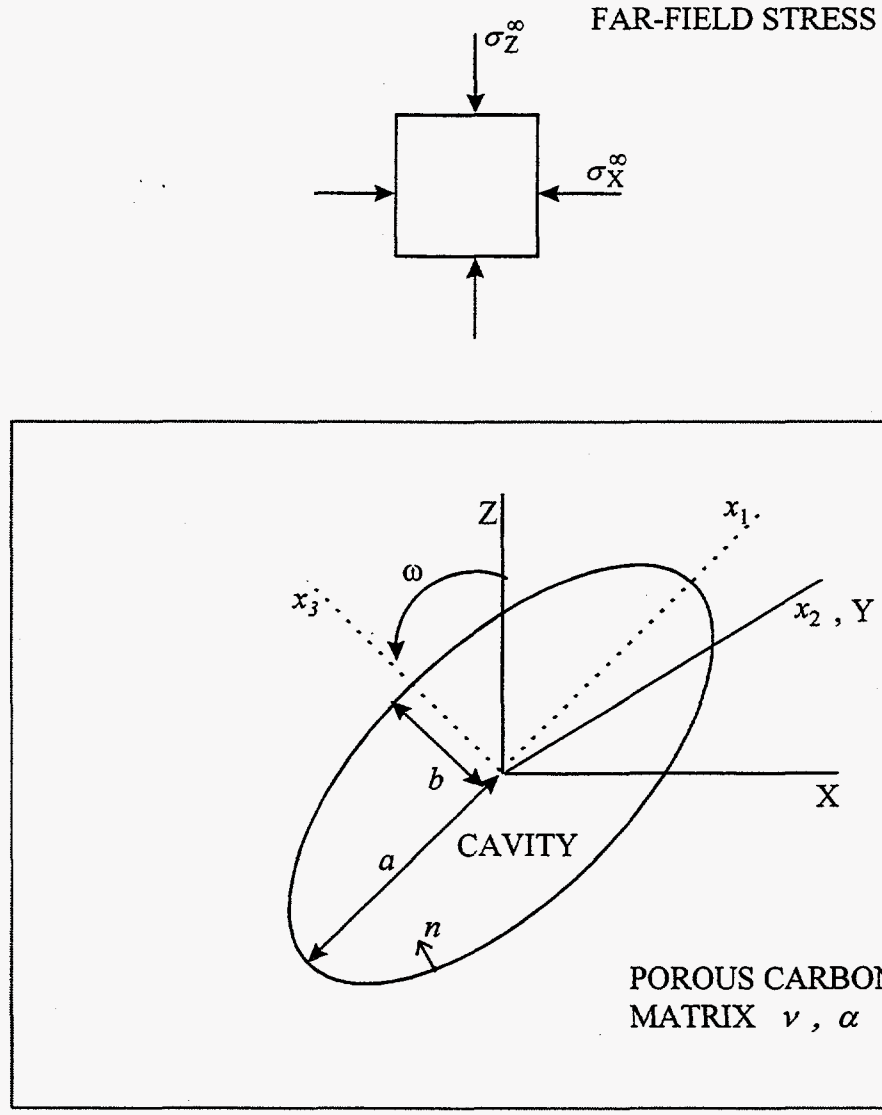
FAR-FIELD STRESS
σ_Z^∞
σ_X^∞
Z
x_1
ω
x_3
x_2 , Y
b
X
a
CAVITY
n
POROUS CARBONATE
MATRIX ν , α

Fig. 1

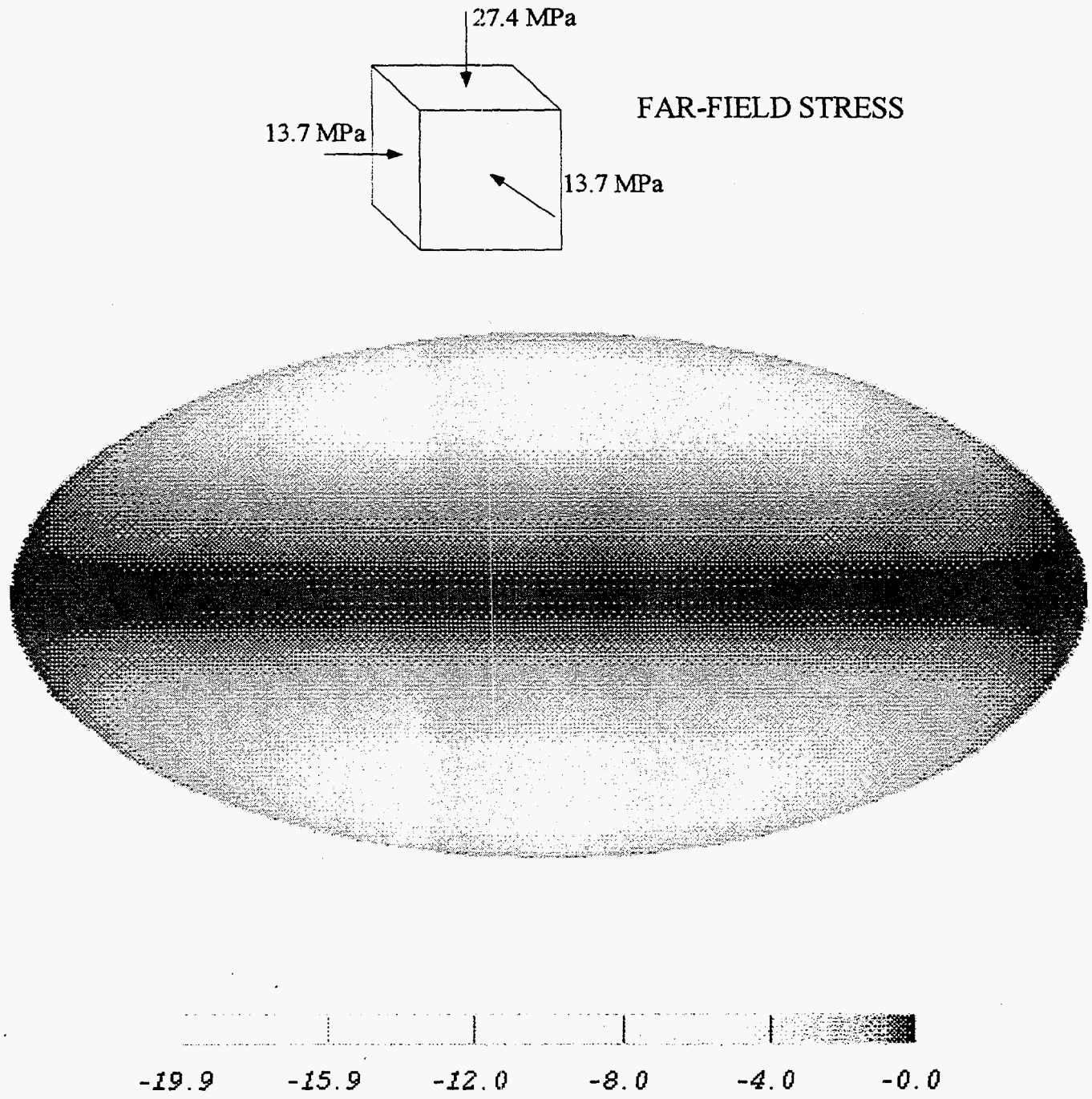

Fig. 2a

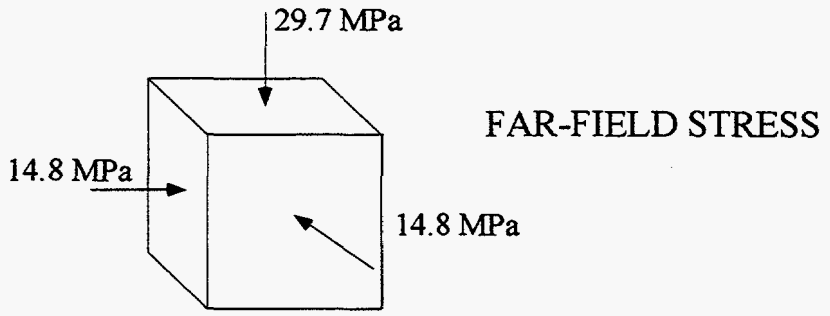

FAR-FIELD STRESS

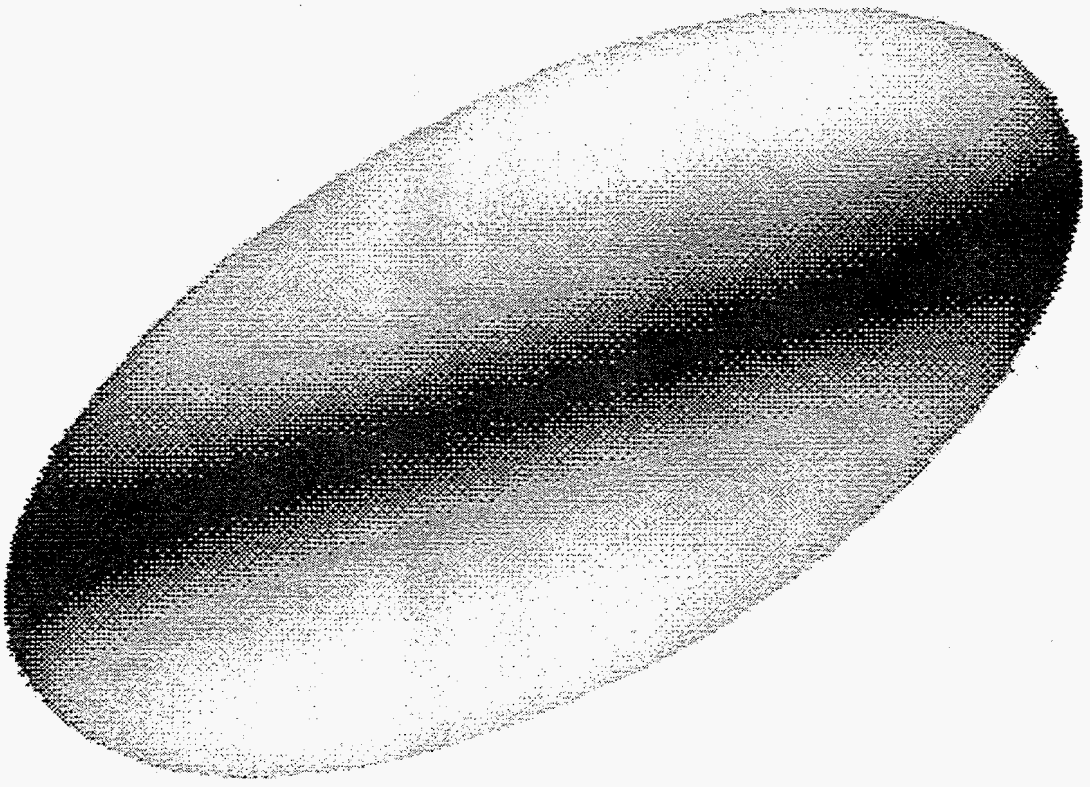

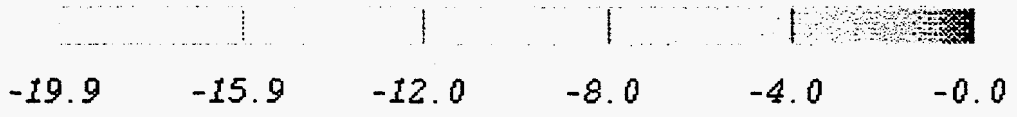

Fig. 2b

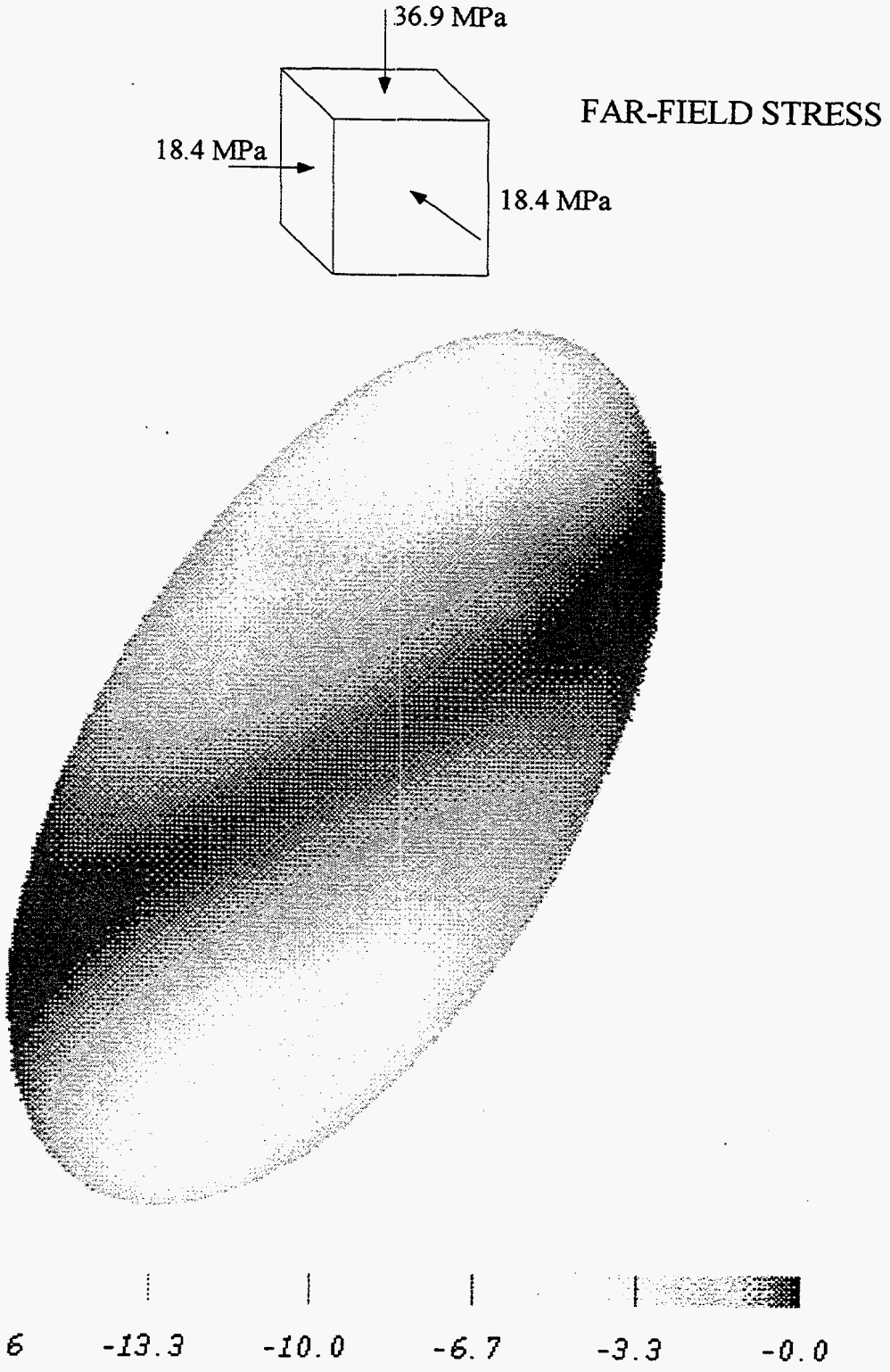

Fig. 2c

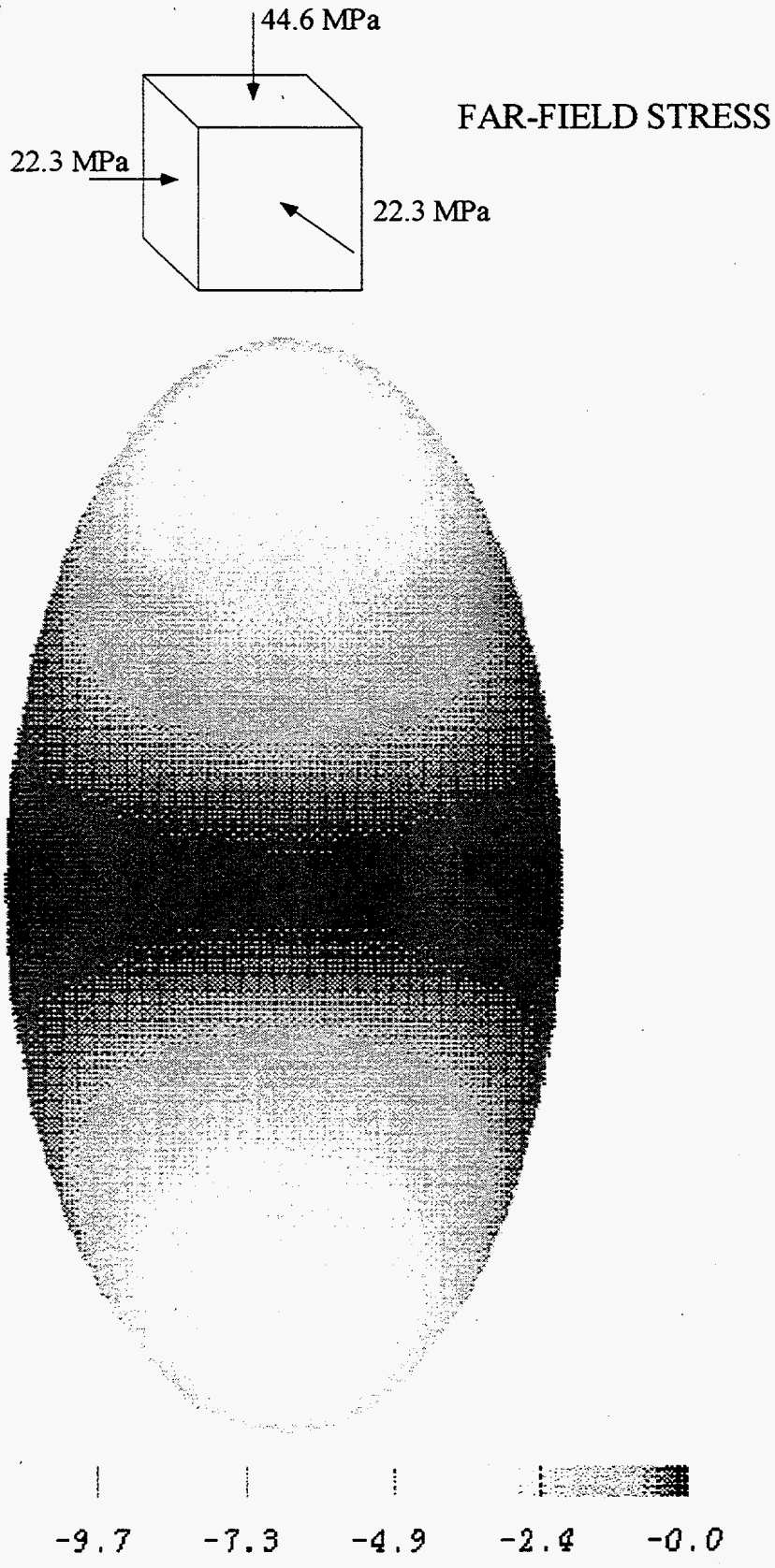

Fig. 2d

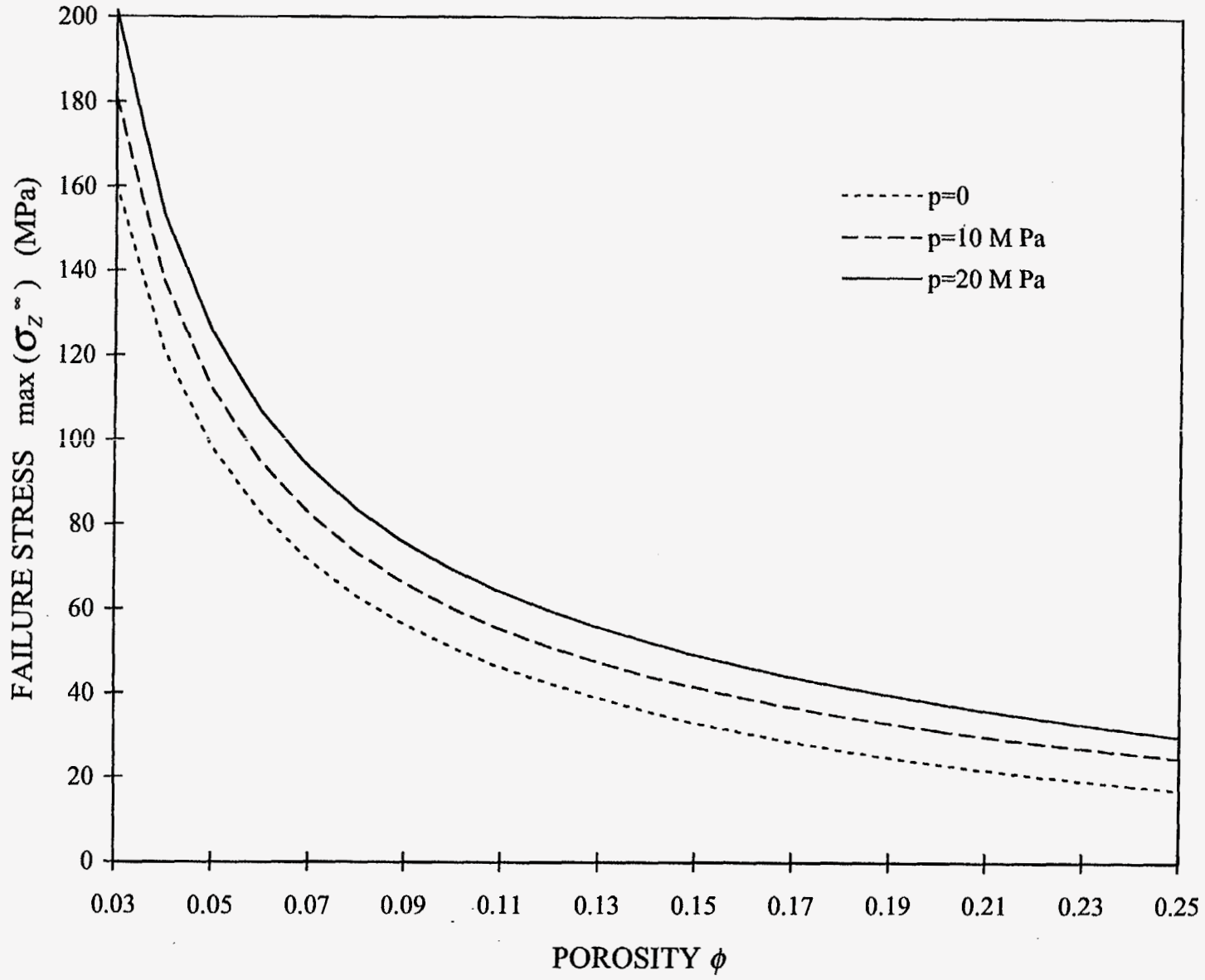
200
180
160
140
120
100
80
60
40
20
0
FAILURE STRESS max (σ_z^∞) (MPa)
p=0
p=10 M Pa
p=20 M Pa
0.03
0.05
0.07
0.09
0.11
0.13
0.15
0.17
0.19
0.21
0.23
0.25
POROSITY ϕ

Fig. 3

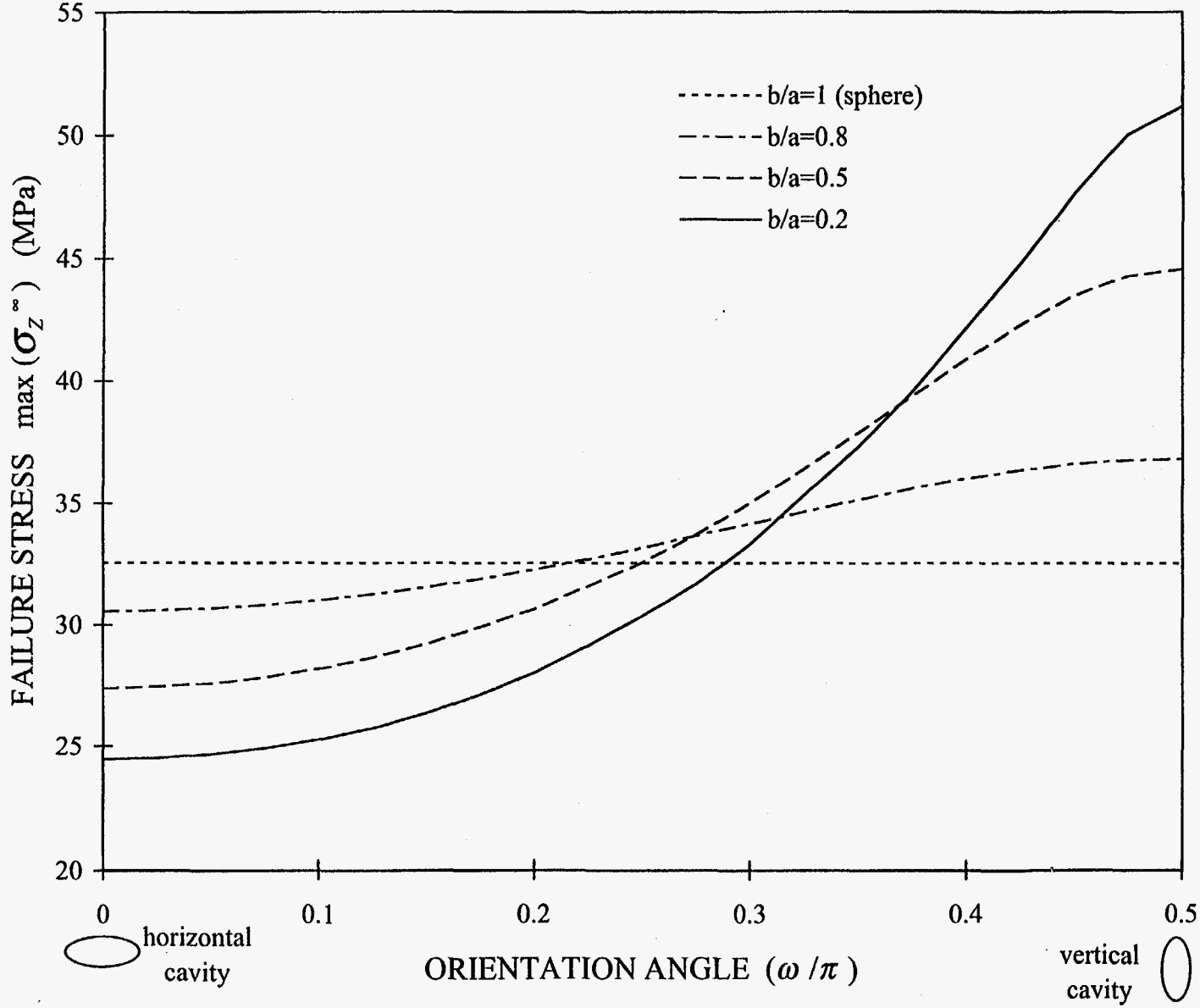
55
50
45
40
35
30
25
20
FAILURE STRESS max (σ_z^∞) (MPa)
b/a=1 (sphere)
b/a=0.8
b/a=0.5
b/a=0.2
0
0.1
0.2
0.3
0.4
0.5
horizontal cavity
ORIENTATION ANGLE (ω/π)
vertical cavity

Fig. 4

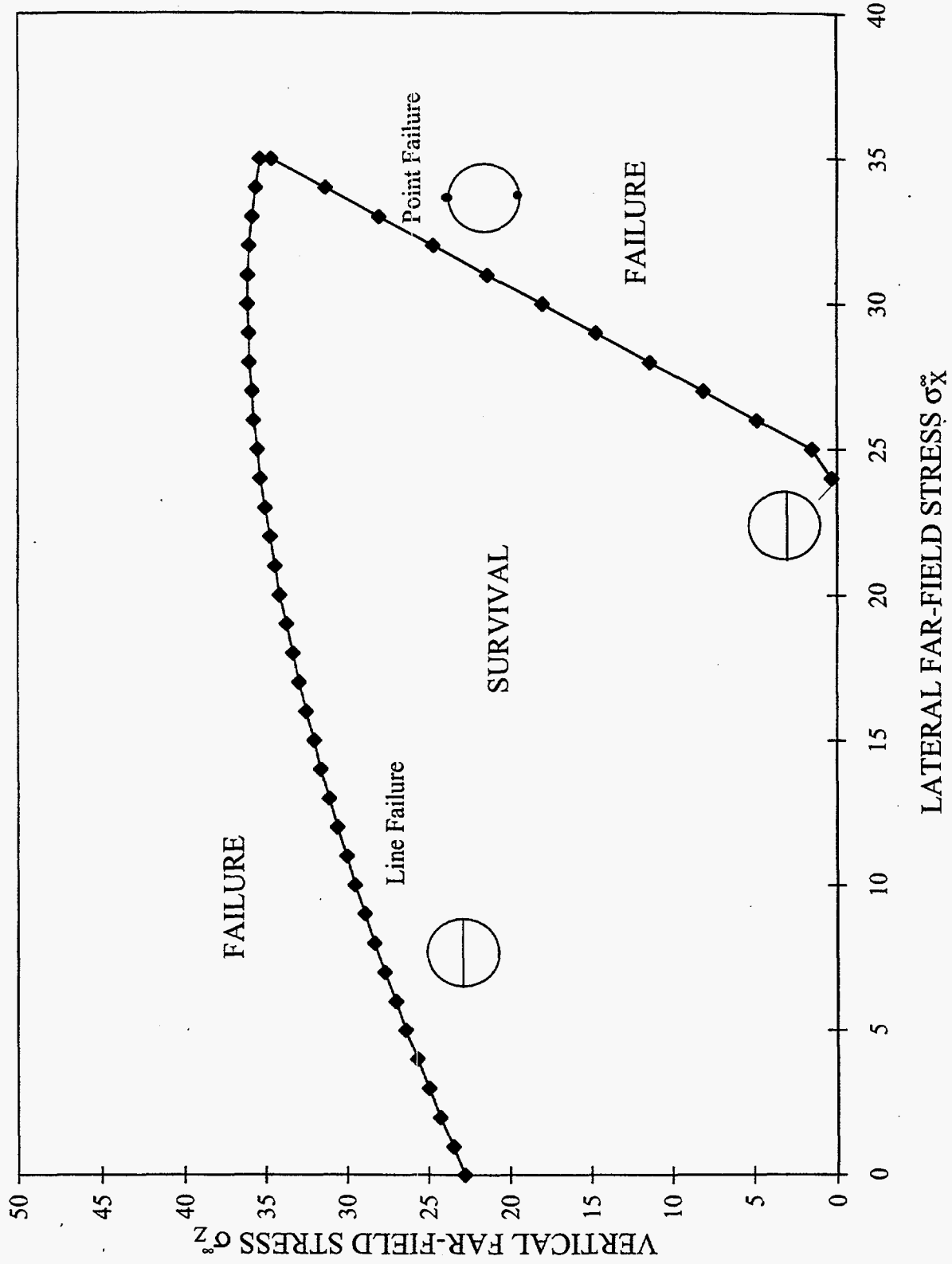
VERTICAL FAR-FIELD STRESS σ^{∞}_{Z}
LATERAL FAR-FIELD STRESS σ^{∞}_{X}
0
5
10
15
20
25
30
35
40
45
50
FAILURE
Line Failure
SURVIVAL
Point Failure
FAILURE

Fig. 5a

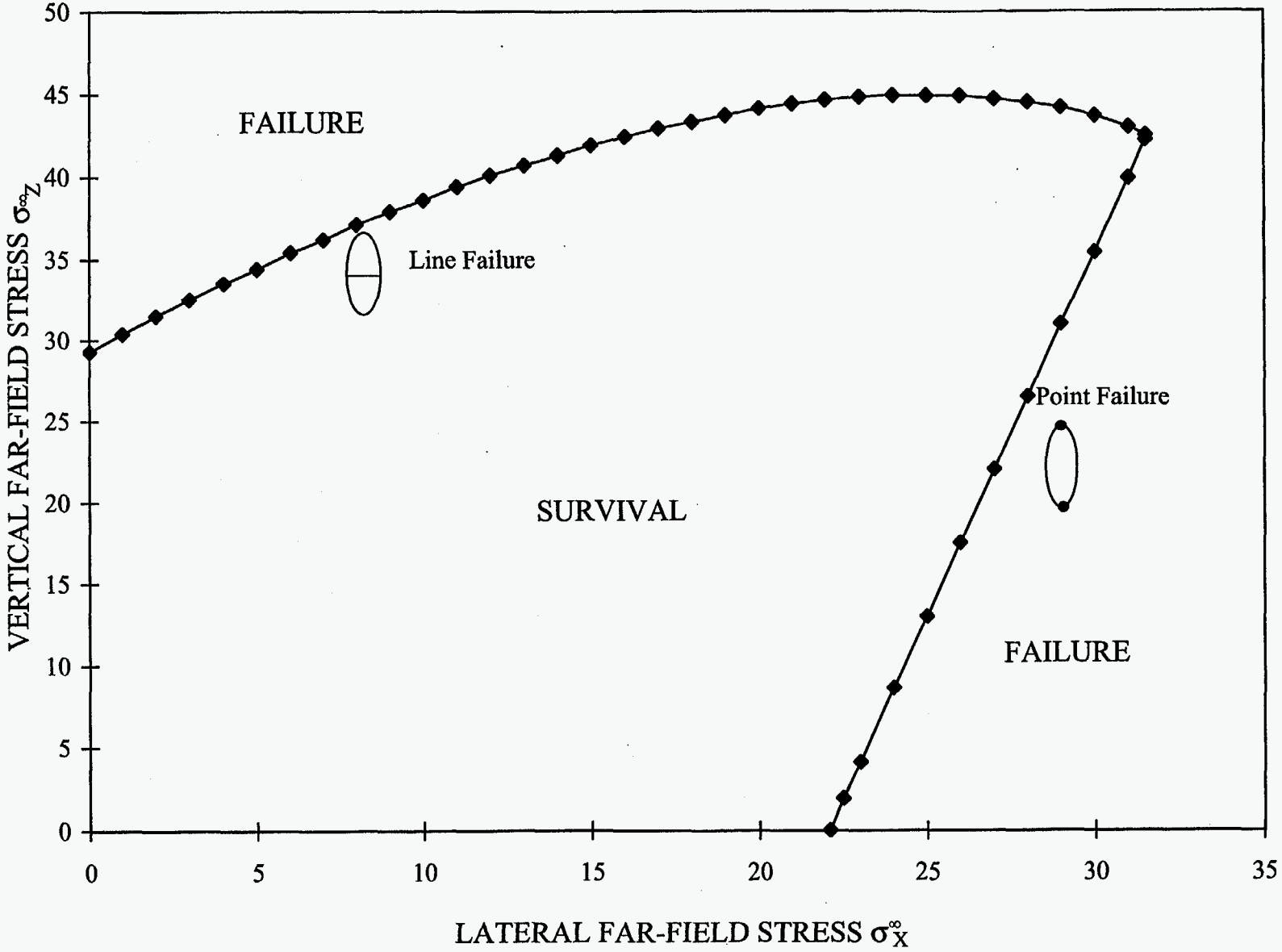
FAILURE
Line Failure
SURVIVAL
Point Failure
FAILURE
VERTICAL FAR-FIELD STRESS σ^{∞}_{Z}
LATERAL FAR-FIELD STRESS σ^{∞}_{X}
0
5
10
15
20
25
30
35
40
45
50

Fig. 5b

VERTICAL FAR-FIELD STRESS σ_z^∞
LATERAL FAR-FIELD STRESS σ_x^∞
FAILURE
SURVIVAL
FAILURE
Point Failure
Point Failure
Point Failure
0
5
10
15
20
25
30
35
40
45
50

Fig. 5c

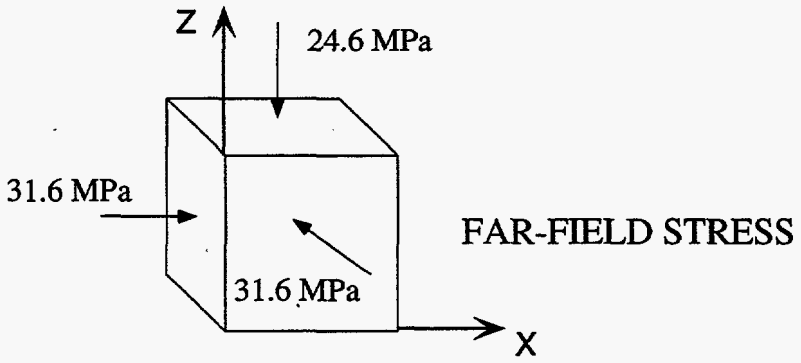

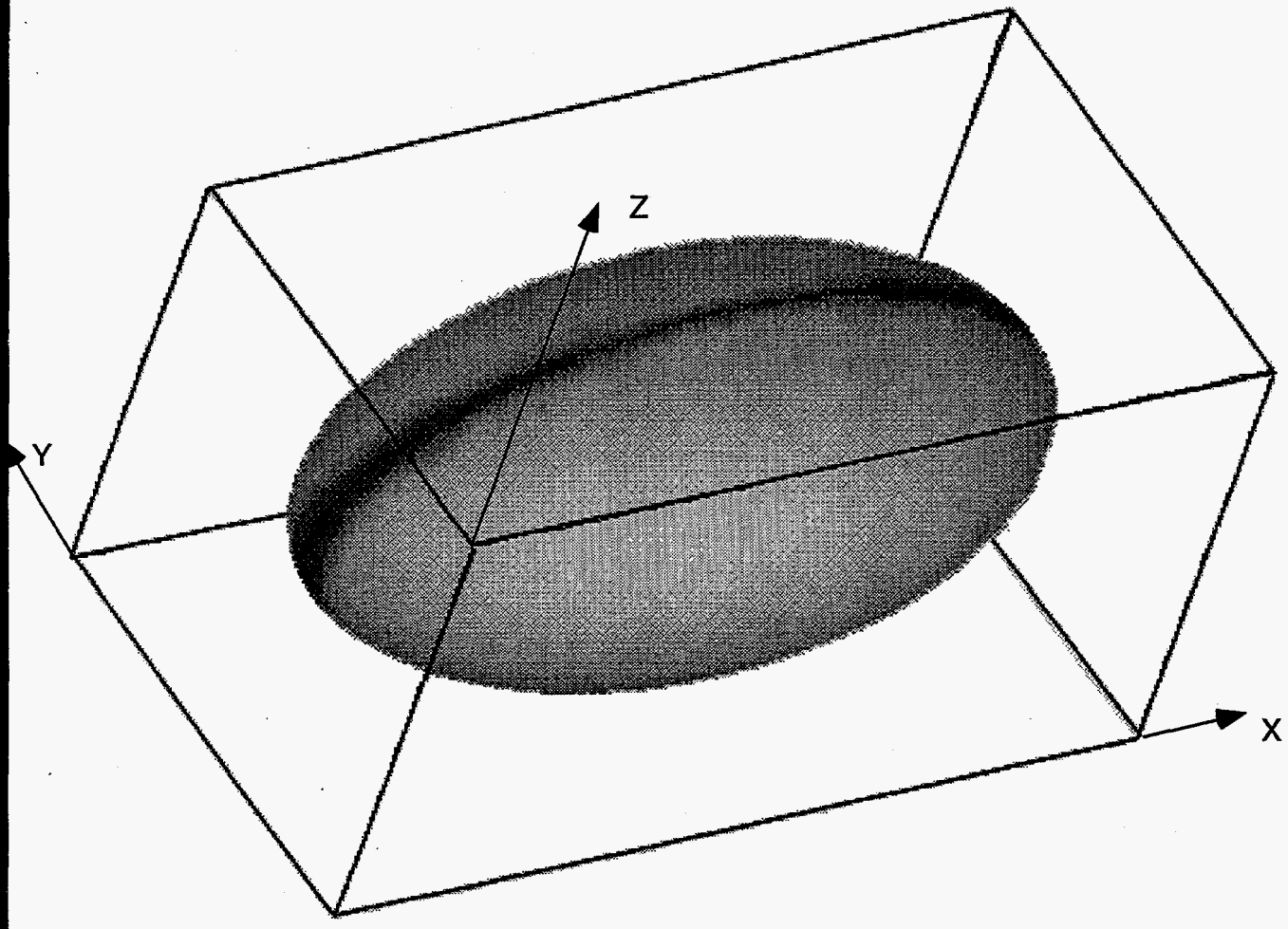

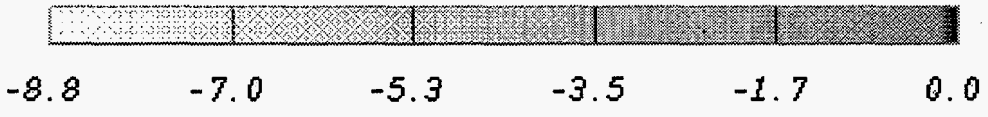

Fig. 5d

Fig. 6

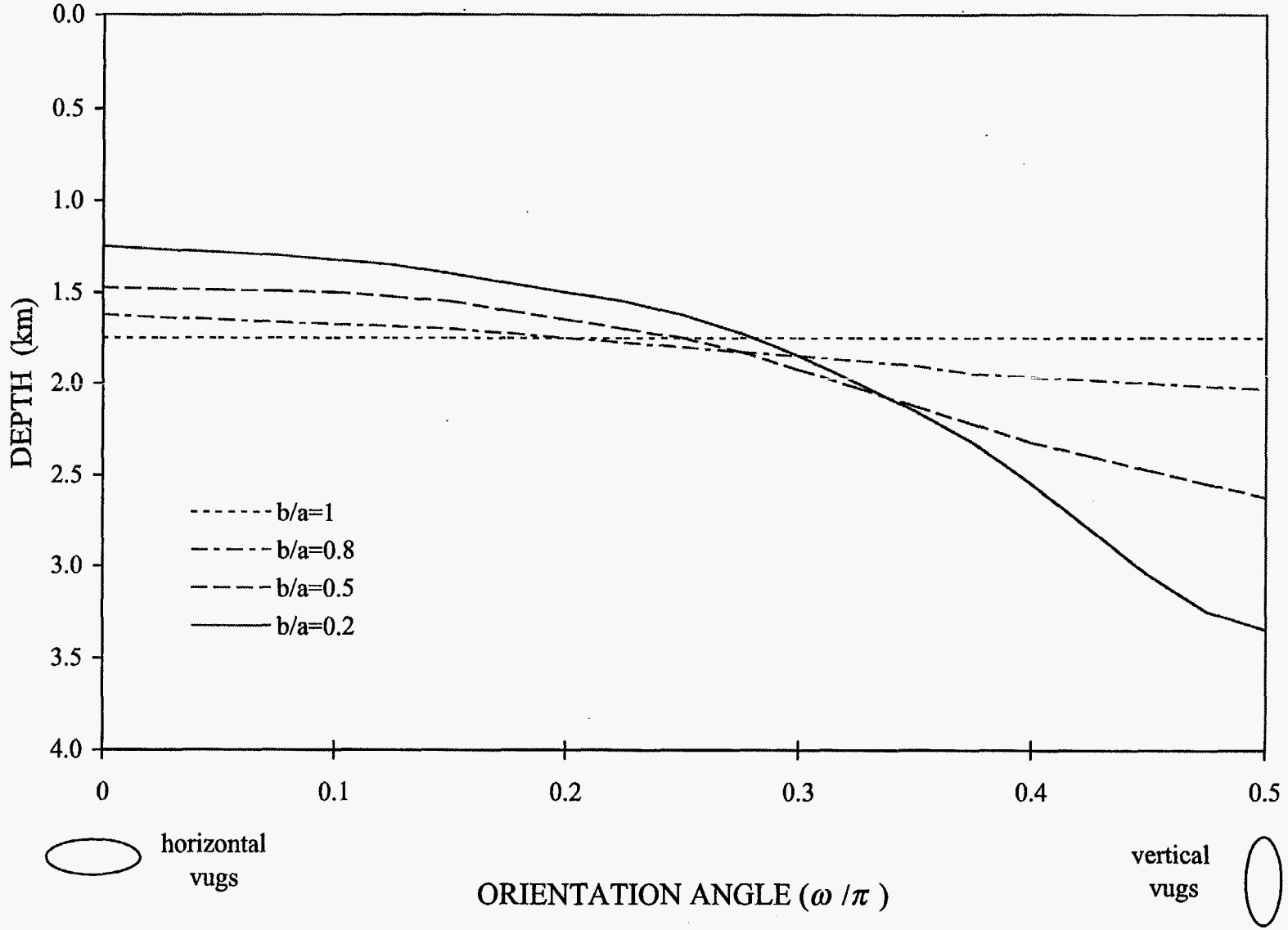
0.0
0.5
1.0
1.5
2.0
2.5
3.0
3.5
4.0
DEPTH (km)
b/a=1
b/a=0.8
b/a=0.5
b/a=0.2
0
0.1
0.2
0.3
0.4
0.5
horizontal vugs
vertical vugs
ORIENTATION ANGLE (ω /π)

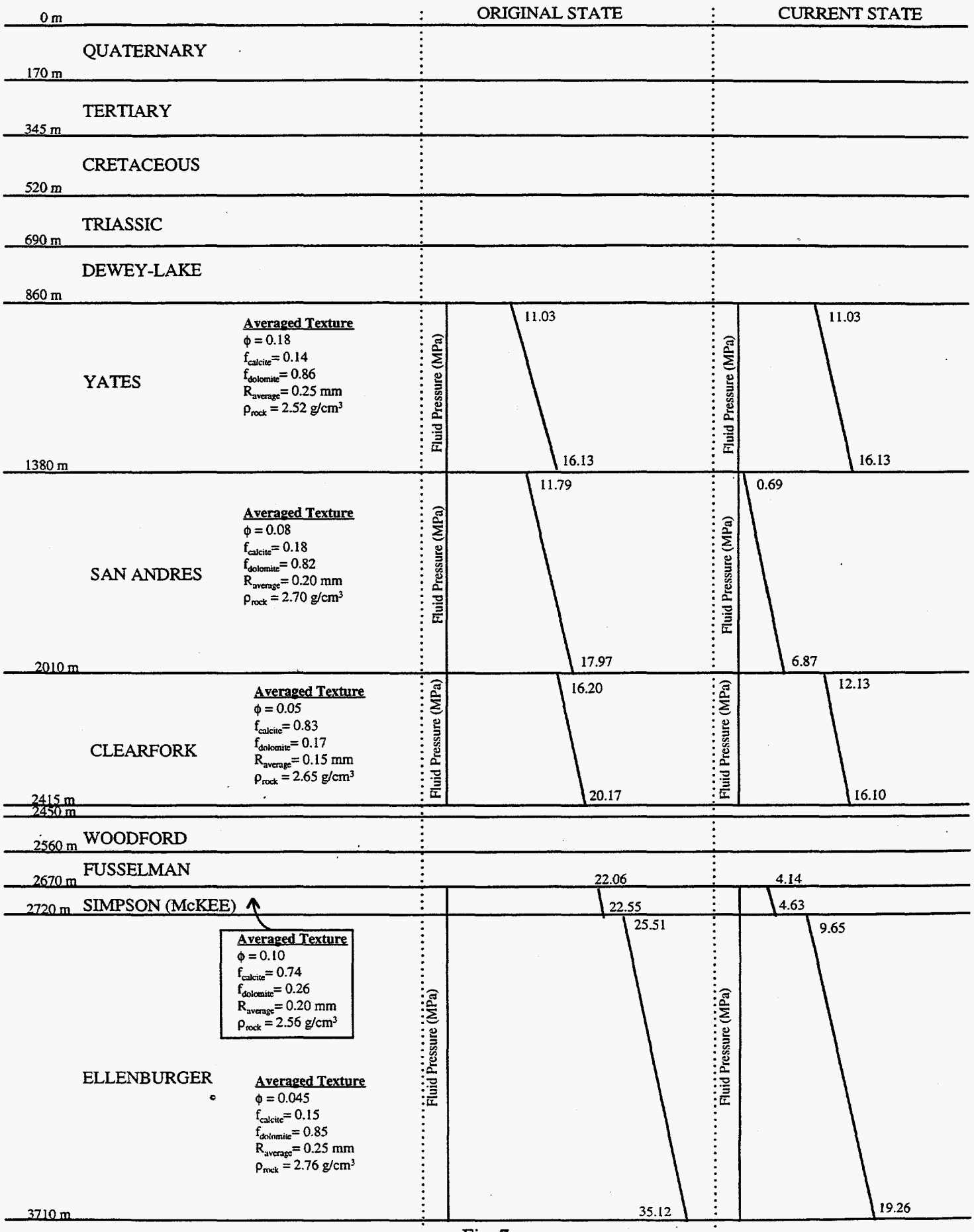
0 m
ORIGINAL STATE
CURRENT STATE
QUATERNARY
170 m
TERTIARY
345 m
CRETACEOUS
520 m
TRIASSIC
690 m
DEWEY-LAKE
860 m
YATES
Averaged Texture
ϕ = 0.18
f_calcite = 0.14
f_dolomite = 0.86
R_average = 0.25 mm
ρ_rock = 2.52 g/cm³
1380 m
SAN ANDRES
Averaged Texture
ϕ = 0.08
f_calcite = 0.18
f_dolomite = 0.82
R_average = 0.20 mm
ρ_rock = 2.70 g/cm³
2010 m
CLEARFORK
Averaged Texture
ϕ = 0.05
f_calcite = 0.83
f_dolomite = 0.17
R_average = 0.15 mm
ρ_rock = 2.65 g/cm³
2415 m
2450 m
WOODFORD
2560 m
FUSSELMAN
2670 m
SIMPSON (McKEE)
2720 m
Averaged Texture
ϕ = 0.10
f_calcite = 0.74
f_dolomite = 0.26
R_average = 0.20 mm
ρ_rock = 2.56 g/cm³
ELLENBURGER
Averaged Texture
ϕ = 0.045
f_calcite = 0.15
f_dolomite = 0.85
R_average = 0.25 mm
ρ_rock = 2.76 g/cm³
3710 m
Fluid Pressure (MPa)
11.03
16.13
11.79
17.97
16.20
20.17
22.06
22.55
25.51
35.12
Fluid Pressure (MPa)
11.03
16.13
0.69
6.87
12.13
16.10
4.14
4.63
9.65
19.26

Fig. 7